We are IntechOpen,
the world's leading publisher of
Open Access books
Built by scientists, for scientists

6,900
Open access books available

186,000
International authors and editors

200M
Downloads

154
Countries delivered to

Our authors are among the

TOP 1%
most cited scientists

12.2%
Contributors from top 500 universities

CLARIVATE ANALYTICS
BOOK CITATION INDEX
INDEXED

WEB OF SCIENCE™

Selection of our books indexed in the Book Citation Index
in Web of Science™ Core Collection (BKCI)

Interested in publishing with us?
Contact book.department@intechopen.com

Numerical Modelling to Understand Cracking Phenomena During Laser-GMA Hybrid Welding Nickel-Base Superalloys

Zhiguo Gao

Additional information is available at the end of the chapter

http://dx.doi.org/10.5772/47395

1. Introduction

Laser welding is a highly efficient and precise welding method, which is greatly desired in the automotive, aero and ship building industries. It elucidates some excellence, such as higher depth to width ratio, concentrated heat input, minimal thermal distortion, minimized weld fusion and heat affected zone, reduced post weld rework and possibly joining widely dissimilar materials. But laser welding has also clearly demonstrated some drawbacks. First of all, the cost of laser equipment and maintenance are high. Second, highly reflective materials, such as aluminum, copper and gold, are more difficult to process with some laser sources. Finally, the high welding speed leads to high solidification rate, which in turn induces metallurgical problems, such as cracking, pores and brittle phase structures.

Laser-gas metal arc (GMA) hybrid welding is one of the state-of-the-art technologies and is designed to overcome problems commonly encountered during either laser or arc welding. Hybrid welding offers some additional advantages over mere laser and arc welding. Firstly, the combination of a laser beam and gas metal arc in welding will reduce the propensity for cracking, brittle phase formation and porosity. Secondly, the feeding wire modifies the metallurgy of the weld. Thirdly, the effect of the coupled process exceeds the effects of the laser and arc heat sources taken separately, and the laser beam located in front of the GMA weld pool could suppress hump formation during high travel speed (Claus et al., 2005; Gao et al., 2009; Ribic et al., 2009).

Nickel-base superalloys are extensively used as aeronautical material due to their high temperature properties. However, commonly used types of commercial welding for nickel-

base superalloys have three major hurdles that need to overcome in order to make refurbishment and repair feasible. First, the single crystal nature of nickel-base superalloys is easily lost during welding due to stray grain formation. This phenomenon is called a columnar-to-equiaxed transition (CET). Secondly, polycrystalline nickel-base superalloys are very prone to cracking during welding, and these cracks are mostly thermally induced cracks which originate in the grain boundary in the heat affected zone (HAZ). The combination of welding stress and increased concentration of gamma-prime are thought to be the cause of hot cracks in the HAZ. Finally, on-equilibrium solidification, elemental partitioning and subsequent solid state transformation can yield non-ideal microstructures and will not produce material with the desired properties.

It has been found that the mechanical strengths at elevated temperatures of columnar grains are better than those of gas turbine blades with equiaxed grains. Columnar grains are desirable, and equiaxed grains are treated as casting defects in directionally solidified or single crystal castings. Some researchers have implemented theoretical analyses on the solidification behaviours of nickel-base superalloys. Hunt (1984) and Gäumann et al. (2001) theoretically analyzed stray grain formation to consider the parameter Φ for describing the extent of nucleation and growth for stray grain formation ahead of the advancing solidification front. Φ represents the volume fraction of equiaxed grains and varies from 0 to 1. The value of Φ can be calculated by the following equation:

$$\frac{G^n}{V} = a \left\{ 3\sqrt{\frac{-4\pi N_0}{3\ln(1-\Phi)}} \frac{1}{n+1} \right\}^n \tag{1}$$

where G is the thermal gradient, V is the growth velocity, a and n are material constants and N_0 is the nucleation density. $a = 1.25 \times 10^6 \text{K}^{3.4}\text{m}^{-1}\text{s}^{-1}$, $n = 3.4$ and $N_0 = 2 \times 10^{15}\text{m}^{-3}$ are used for a similar nickel-base superalloy. When constitutional supercooling is minimal, $\Phi = 0$, the weld microstructure is free of stray grains and maintains its single crystal nature. When $\Phi = 1$, solidification is equiaxed. A critical value of Φ that corresponds to a stray grain free microstructure is hypothesized to be 0.0066.

Gäumann et al. (2001) derived a criterion based on the G^n/V ratio which states that the microstructure is columnar when the following condition is satisfied everywhere in the weld melt pool.

$$\frac{G^{3.4}}{V} > 2.7 \times 10^{24} \left(\text{K}^{3.4}/\text{m}^{4.4}\text{s} \right) \tag{2}$$

Park et al. (2003) used the degree of constitutional supercooling (CS) at the solidification front as a metric to assess the effects. The basic criterion to avoid CS, which leads to the growth of new grains at the solidification front, is given by:

$$\frac{G}{V} > \left(\frac{G}{V}\right)_{cr} \tag{3}$$

where $(G/V)_{cr}$ is a critical value of G/V, which is proportional to $\Delta T/D_L$ (ΔT is the solidification temperature range, and D_L is the diffusion coefficient of solute in the liquid). In cases where the planar solid/liquid interface breaks down into cellular or dendritic solidification, the theory of CS predicts fairly closely. However, no theory can predict the $(G/V)_{cr}$ for the CET.

Liu and DuPont (2004, 2005) studied the effects of melt-pool geometrical parameters on crystal growth and microstructure development during laser surface melting of single-crystal alloys.

Thanks to the development of welding techniques, much progress has been made to discuss cracking phenomena in the laser join nickel-base superalloys (Egbewande et al., 2010; Hong et al., 2008; Liu et al., 2011). Recently, feasible finite element models were established to provide substantial insights into cracking and how thermal gradient, transient stress and strain were developed in the laser welding process (Dai&Shaw,2001; Hee et al.,2010; Hu&Richardson,2006;Long et al.,2008;Luo et al.,2002; Nishimoto et al., 2002; Wang et al., 2004; Yann et al.,2010 ;Yilbas et al.,2010).

As mentioned previously, albeit laser welding is achieved by rapid heating and rapid cooling, solidification cracking and liquation cracking are prone to be generated in the weld and HAZ. The effect of weld pool shape on the solidification cracking and HAZ cracking susceptibility still remain obscure in many respects for the laser welding. Some experimental conclusions from previous literature have proved that the number of micro cracks at the fusion line in the weld cross-section is reduced with increasing heat input for laser-arc hybrid welding, and cracking might be prevented by adjustment of filler material and heat input for the laser-arc hybrid welding. However, limited information and rationale are available in the literature about how the weld solidification cracking and HAZ crack susceptibility are minimized during laser-arc hybrid welding.

In this chapter, in order to properly explore the capability of the new welding process, i.e. laser-arc hybrid welding, it is necessary to know and understand how laser-arc hybrid welding affects solidification cracking and liquation cracking. A major factor control susceptibility to solidification cracking and liquation cracking are stray grain formation and stress-strain generation during weld pool solidification, respectively. It is important to study and understand stray grain formation and stress-strain generation mechanism during laser-arc hybrid welding, whereas these information are currently scarce in the literature.

2. Solidification cracking and liquation cracking modeling

In this section two kinds of theoretical analysis models are developed to understand cracking phenomena, one is modelling analysis of hybrid laser-arc welding of single-

crystal nickel-base superalloys and the other is modelling analysis HAZ liquation cracking of laser hybrid welding polycrystalline nickel-base alloy and schematic diagram is shown in Fig.1.
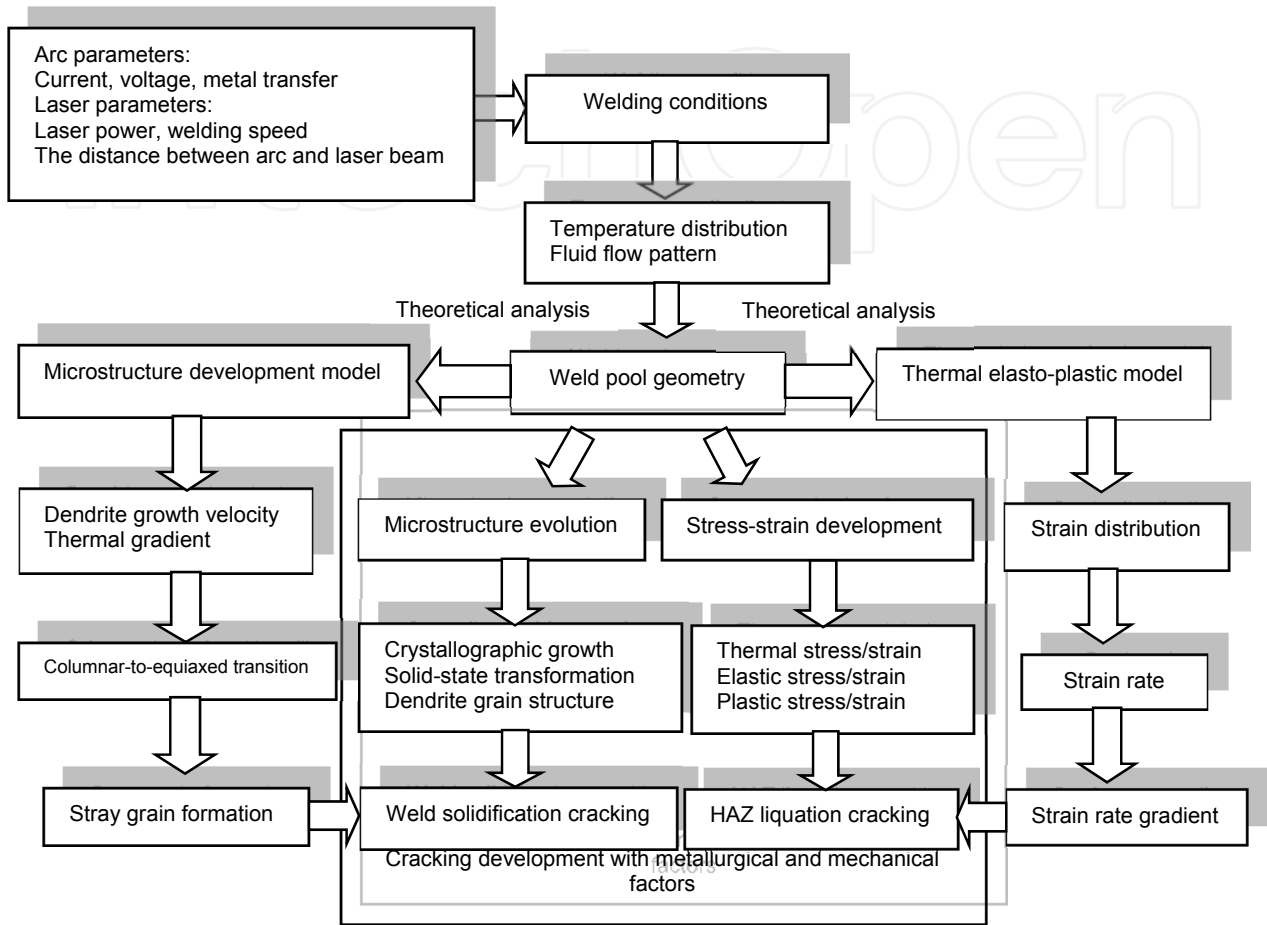

Figure 1. Schematic diagram of cracking development and theoretical analysis for the laser-GMA hybrid welding nickel-base superalloys

2.1. Solidification cracking modeling for single-crystal superalloys welding

2.1.1. Mathematical model description

To execute the analysis on the dynamic behavior and solidification of molten pool, three-dimensional essential governing equations, such as continuity, Navier-Stokes, energy and VOF method equations are iteratively solved with the assumption that the liquid flow is Newtonian, laminar and incompressible.

Continuity equation

$$\nabla \cdot V \rho_l = \dot{m}_s \qquad (4)$$

Momentum equation

$$\rho_l\left(\frac{\partial V}{\partial t} + V \cdot \nabla V\right) = \mu \nabla^2 V - \nabla P + \dot{m}_s \cdot V + F - KV \tag{5}$$

Energy equation

$$\rho_l\left(\frac{\partial (U)}{\partial t} + V \cdot \nabla (U)\right) = \nabla \cdot (k_l \nabla T) + \dot{U}_s \tag{6}$$

$$U = \int_T c(T)dT + (1 - f_s)h_{st} \tag{7}$$

where V is the molten metal velocity, $\dot{m}_s$ is a mass source term, P is the hydrodynamic pressure, μ is the dynamic viscosity, F is the body force, ρ_l is the fluid density, U is internal energy per unit mass, k_l is thermal conductivity, T is a local temperature, $\dot{U}_s$ is an energy source term due to mass source term, K is the drag coefficient for the porous media model, f_s is the solid fraction, and c (T) is specific heat.

According to the kinematic motion equation, the VOF function moves according to the velocity field in the fluid, as shown by Equation (8).

$$\frac{\partial F}{\partial t} + \nabla \cdot (VF) = \dot{F}_s \tag{8}$$

For a single fluid, incompressible problem F represents the volume fraction occupied by the fluid. Thus, fluid exists where F=1, and void regions correspond to locations where F=0. $\dot{F}_s$ represents the change of volume fraction of fluid associated with the mass source .

The local temperature gradient G_{hkl} and dendrite growth velocity V_{hkl} can be calculated to predict the microstructure development across the entire solidification interface. The solidification front produced at the rear part of the weld pool is identified by a solidus curve. The effect of keyhole penetration on weld pool geometry is considered in the analysis of the microstructure development. Fig. 2 illustrates a schematic diagram of the weld pool and associated geometry variables, which illustrate the relationships among the welding velocity $\vec{V}_b$, the solidification front unit vector $\vec{n}$, and the dendrite growth velocity $\vec{V}_{hkl}$. Ψ is the angle between the solidification front normal $\vec{n}$ and a particular dendrite growth direction [hkl]. θ is the angle between the surface normal $\vec{n}$ and the welding direction, and ϕ is the angle between the y-axis and the projection of $\vec{n}$ on the y-z plane. L_{al} is the distance between the laser beam and GMA, c_l and c_a are the penetration of laser and arc welds, respectively.

Based on previous analytical methods(Liu&DuPont,2004,2005; Rappaz et al.,1990), a mathematical model is extended for the calculation of stray grain fraction during solidification microstructure development in the hybrid weld pool. The 3-D melt-pool geometry on the rear part of the weld can be described in an ellipsoid formula.

$$\frac{x^2}{a^2} + \frac{y^2}{b^2} + \frac{z^2}{c^2} = 1 \qquad (9)$$

where a, b and c are the half-axes of the ellipsoid in the x, y and z directions, respectively. As well, a is the length between the location of the maximum width and trailing point, b is the maximum width of the arc pool, c is the maximum depth and in consideration of the solidification history of weld pool penetration, c_l is used in this model.

The relationship of the velocity of the dendrite tip, $\vec{V}_{hkl}$, along a specific [hkl] direction is given by:
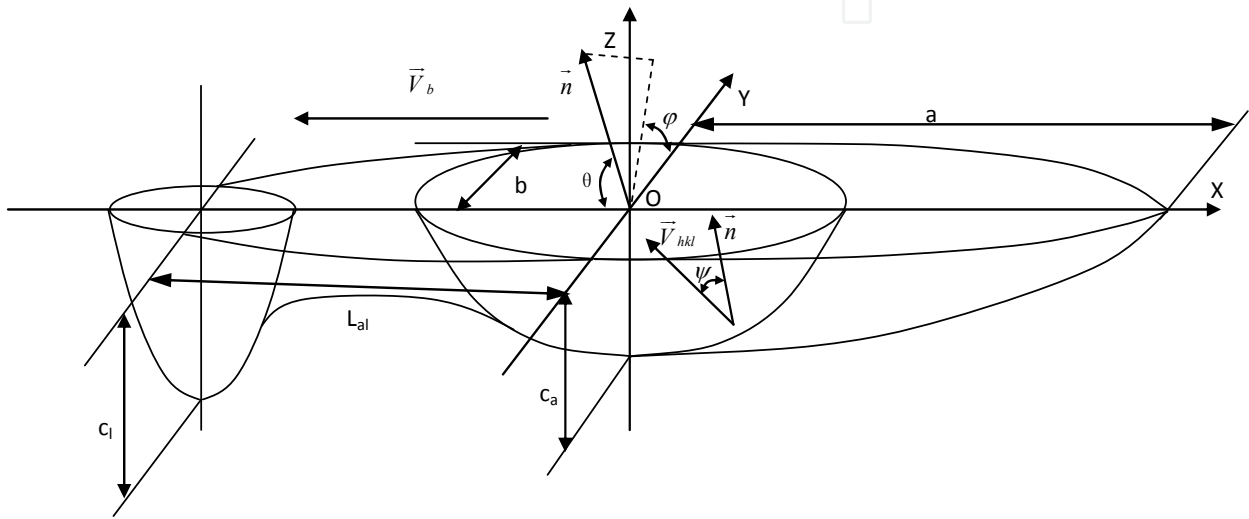

Figure 2. Schematic diagram of weld pool geometry mathematical model and associated variables (Gao&Ojo,2012a)

$$\left|\vec{V}_{hkl}\right| = \frac{\left|\vec{V}_n\right|}{\cos\psi} = \left|\vec{V}_b\right|\frac{\cos\theta}{\cos\psi} \qquad (10)$$

where $\vec{V}_n$ is the growth rate of the normal to the solidification front at the liquid-solid interface.

The unit component based on the weld pool normal in the x, y and z axes are determined by

$$\vec{n} = \left(\cos\theta, \sin\theta\cos\varphi, \sin\theta\sin\varphi\right) \qquad (11)$$

In order to determine the growth velocity along the [hkl] dendrite growth direction (one of the six <100> directions), the value of $\cos\psi$ can be determined from the relation:

$$\cos\psi = h\cdot\cos\theta - k\cdot(\sin\theta)(\cos\varphi) + l\cdot(\sin\theta)(\sin\varphi) \qquad (12)$$

The thermal gradient along the dendrite growth direction, $\vec{G}_{hkl}$, is given by the expression:

$$\left|\vec{G}_{hkl}\right| = \left|\vec{G}_n\right|\cos\psi \qquad (13)$$

where $\left|\vec{G_n}\right|$ is the total thermal gradient direction in the x, y and z directions.

The expression is solved for the volume fraction of stray grains Φ as a function of G_{hkl} and V_{hkl} which yields:

$$\Phi = 1 - e^S \tag{14}$$

$$S = \frac{-4\pi N_0}{3}\left(\frac{1}{(n+1)\left(G^n/aV\right)^{1/n}}\right)^3 = -2.356\times10^{19}\left(\frac{V_{hkl}}{G_{hkl}^{3.4}}\right)^{3/3.4} \tag{15}$$

The area-weighted average across the entire solidification interface, $\overline{\overline{\Phi}}$, is given by the expression:

$$\overline{\overline{\Phi}} = \frac{\sum_k A_k \overline{\Phi}}{\sum_k A_k} \tag{16}$$

where the variable k corresponds to the cross-section along the x axis, and A_k and $\overline{\Phi}$ are the areas and average Φ values for each cross-section, respectively. More information about this numerical model can be reviewed by the reference (Gao&Ojo,2012a).

Thermal properties of typical nickel-base alloy used in this model are directly taken from values produced in the previous literatures(Anderson et al.,2010; Banarjee&Overfelt,1999; Bonifaz&Richards,2009; Brooks et al.,1996; Luo et al.,2002; Pottlacher et al.,2002; Zeng,2006), and are presented in Table 1.

Material property	Value	Unites
Density of liquid	7578.9	Kg m^{-3}
Density of solid	7742.5	Kg m^{-3}
Viscosity of liquid	0.0074	Kg.s/m
Solidus temperature	1507	K
Liquidus temperature	1613	K
Specific heat of solid	430	J kg^{-1}K^{-1}
Specific heat of liquid	700	J kg^{-1}K^{-1}
Thermal conductivity of solid	11.4	Wm^{-1}K^{-1}
Thermal conductivity of liquid	28.7	Wm^{-1}K^{-1}
Coefficient of thermal expansion	1.33×10^{-5}	K^{-1}
Latent heat of fusion	1.45×10^5	J kg^{-1}
Latent heat of vaporization	6.4×10^6	J kg^{-1}
Surface tension	1.8	N m^{-1}
Surface tension gradient	-1.37×10^{-3}	N m^{-1}k^{-1}

Table 1. Nickel-base alloy properties used in this model

2.1.2. Results and discussion

The material adopted for this simulation is a nickel-base superalloy with a thickness of 3 mm. The focal plane of the laser beam is placed on the top surface of the base metal. Arc droplets are assumed to be steadily generated through a certain wire feed rate at an initial speed of 1.5m/s, and initial temperature 1613K. The size of the droplet mainly depends on the diameter of the feeding wire, and the generation frequency is determined by the wire feed rate and wire diameter. The distance between the arc source and laser beam is 3 mm, and the different welding conditions are listed in Table 2.

	Current (A)	Voltage (V)	Laser power (W)	Welding velocity (m s^{-1})	Droplet frequency (Hz)	Arc heat distribution parameter(mm)
Weld1	120	21	3667	0.022	217	2.23
Weld2	150	21	3667	0.022	269	2.33
Weld3	180	21	3667	0.022	304	2.45
Weld4	120	21	3667	0.028	217	2.23
Weld5	120	21	3667	0.034	217	2.23
Weld6	120	21	4000	0.022	217	2.23
Weld7	120	21	4332	0.022	217	2.23

Table 2. List of Hybrid welding parameters used for Nickel-base superalloy (Gao&Ojo,2012a)

2.1.2.1. Role of welding parameters on microstructure development

The properties of weld metal are affected by solidification behavior parameters, such as growth rates, temperature gradients, undercooling and alloy constitution, which are often useful to determine the development of microstructures in weld zones (Farzadi et al., 2010; He et al., 2005; Roy et al., 2006). In this study, the effect of undercooling has been simplified and thereby the solidification parameters, such as cooling rate, thermal gradient, and solidification velocity, are computed by the weld pool geometry considering only the heat transfer and fluid flow.

Since the shape of the weld pool remains constant under a steady-state condition, the solidification rate can be calculated with position along the fusion boundary. The steady state solidification rate, V_n, is related to the welding velocity in the following formula relation:

$$V_n = V_d \cos\theta \tag{17}$$

where θ is the angle between the normal to the solid/liquid boundary and the welding direction, and V_d is the welding velocity. The solidification rate increases from the edge of the weld pool and pool bottom, where θ is nearly 90°, to the weld centerline, where the velocity equates V_d along the fusion boundary (Farzadi et al., 2010).

To remove the constitutional undercooling ahead of the growth front for columnar grain growth, a high thermal gradient is required and low solidification velocities are desired

(Bussac & Gandin, 1997; Dong, 2007). The values of the temperature gradient and solidification rate vary with position along the entire solidification interface of the weld pool. The density of temperature isotherm in the maximum width is greater than that of the trailing portion of the pool boundary, so the temperature gradient is higher at the fusion line than the centerline. The ramifications of cooling rates (G×R) along the solid/liquid interface with different welding conditions are presented in Fig.3.

The cooling rate is higher at the maximum width of the fusion boundary and lower at the weld centerline for each case in Fig.3 (A). It is observed that the average range of the cooling rate is 4×10^3-2.4×10^4 K/s. The magnitude of the cooling rate decreases with an increase in the arc current and laser power, while an opposite effect will occur with a decrease in welding speed. In general, increasing the welding speed or decreasing welding heat sources power will increase the cooling rate, and the latter will result in an increase of residual stress and strain. In addition, the solidification velocities will be high and this may lead to more extensive non-equilibrium solidification and partitioning at high welding speeds (Rai et al., 2007; Vitek, 2005).

The cooling rate along the solid/liquid boundary of penetration in the conjoint zone is shown in Fig.3 (B). It is observed that the magnitude of the cooling rate is 10^5-7×10^5 K/s, which is approximate to the typical laser welding range of 10^4-10^6 K/s (Ral et al., 2009). It is higher at the bottom of the keyhole than that at the weld crown solid/liquid boundary. This distribution is consistent with higher convective heat transfer near the pool surface than the weld root. The Marangoni convection brings fluid from the weld center to the peripheral solid/liquid interface, which yields a lower thermal gradient on the weld pool surface. It can be further found that the value of the cooling rate near the bottom of the keyhole dramatically increases with increase in the arc current, welding speed and laser power, and the effect of laser power is the most obvious. Meanwhile, the magnitude of the cooling rate near the maximum depth of the weld pool is much higher than that of the rear part of the weld pool.
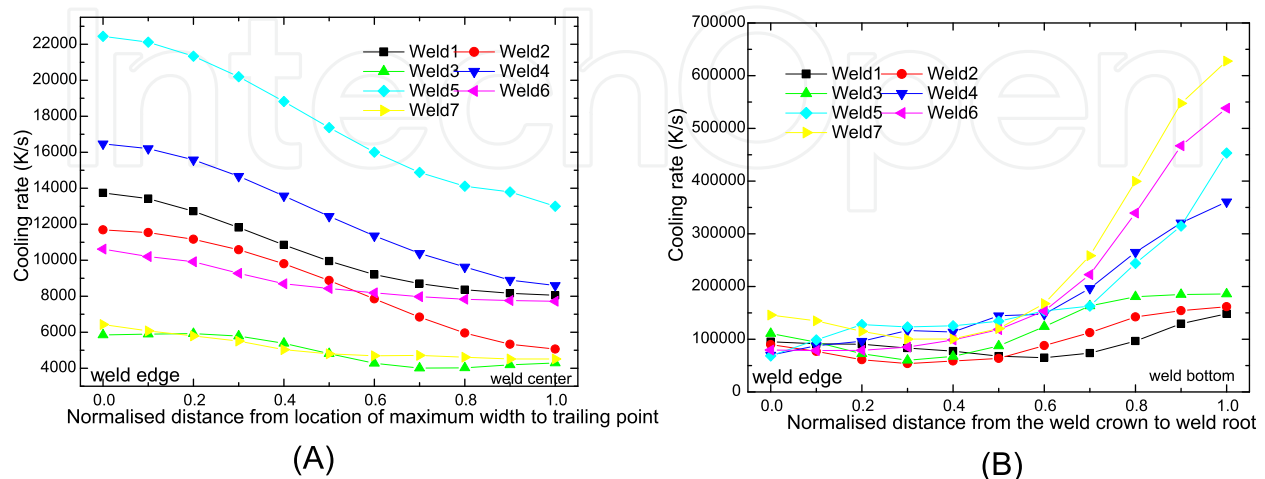

(A)   (B)

Figure 3. The calculated cooling rate along the solidification interface for different welding conditions, (A) Weld pool surface, (B) Weld penetration direction (Gao&Ojo, 2012a)

Secondary dendrite arm spacing (SDAS) is estimated from the cooling rates (G×R).The dendrite arm spacing increases from the interface of maximum weld width to the weld centerline, and decreases from the weld crown to weld root, as shown in Fig.4. These explicate that the finer arm spacing is always found near the fusion boundary on the weld crown or part of the weld root, and the coarsest structure occurs in the center of the weld crown.

As the arc current and laser power were increased, the dendrite trunk spacing along the rear of the solid/liquid interface of the weld pool increases and the magnitude of the SDAS is between 2.88 and 4.2 µm. Dendrite arm spacing decreases with increasing velocity, more obvious for higher welding speed, and the characteristic magnitude of SDAS is between 2.18 and 3.2 µm. The calculated dendrite arm spacing along the solidification interface has the same tendency as the measured values, but the former is slightly greater than the latter, especially near the fusion boundary, see Fig.4 (A).

The SDAS near the solid/liquid boundary along the weld penetration is presented in Fig.4 (B). The dendrite trunk spacing near the root part of the weld gradually decreases with increase in the arc current, welding speed and laser power. The calculated dendrite arm spacing along the direction of weld penetration agrees reasonably well with the measured value near the lower region of the keyhole, and the experiment result is higher in value than that calculated on the weld crown. Hybrid welding allows for the weld metal to remain at a high temperature for a longer time and cool at lower rates compared to approximated laser power performed at the same welding speed (Moore et al., 2004). This results in a coarser dendritic microstructure region where the laser and arc beams simultaneously interact, which is at the weld crown center rather than the solidification boundary.
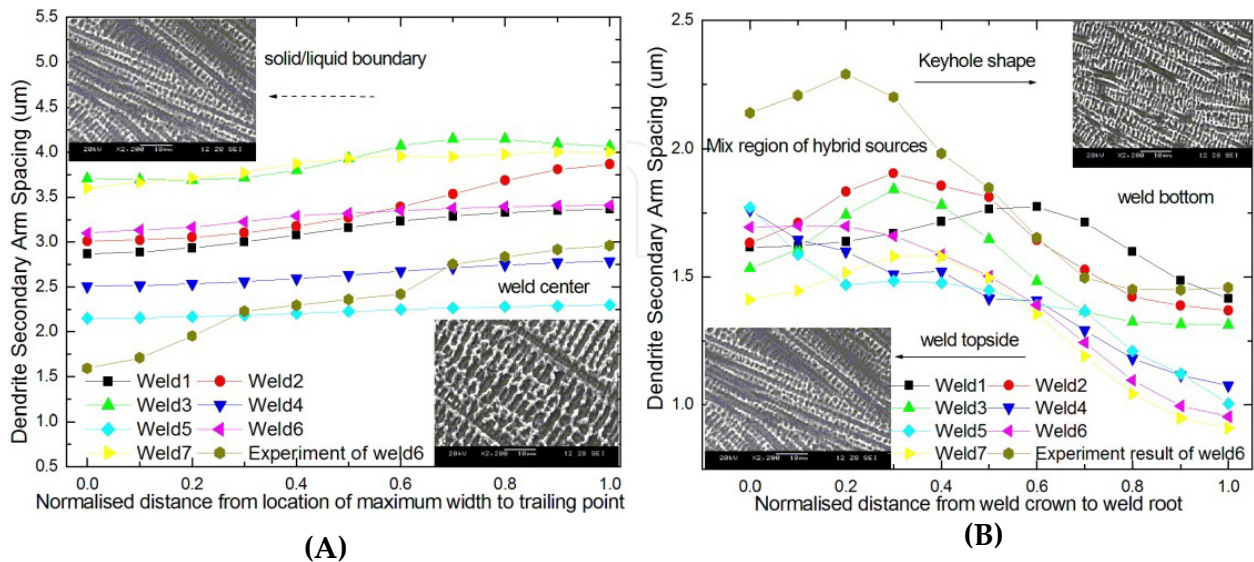

Figure 4. Predicted and experimental results of SDAS along the weld pool solidification interface, (A) Weld pool surface, (B) Weld penetration direction

Since the effect of the crystallographic orientation of the weld on the overall tendency to form stray grains is minimal, the weld direction [100] and sample surface plane (001) are specified for the sample orientation. The angles (θ, ϕ), which characterize the normal to the solidification front, are determined from three-dimension weld geometry, and dendrite growth pattern transitions can occur along the solidification interface. In consideration of the average growth velocity along the solidification interface front at each analysis cross-section, the dendrite orientation velocities of [100], [010] and [001] are presented in Fig.5. The θ, ϕ, ψ terms are used to calculate the dendrite growth velocity by Eqs. (10) and (12). The velocities of the [100] dendrites are always equal to those by welding, regardless of the weld pool shape for the (001) ∥ [100] orientations (Rappaz et al.,1990), and average dendrite tip velocity in [010] and [001] is higher than that of the [100] orientation along the rear part of the solid/liquid interface. The average dendrite tip velocity of the [001] orientation is much larger than that of [010], and the latter is higher than that of [100] near the solidification interface. It can be underlined that $\psi > \theta$ and the dendritic orientation does not coincide with the solidification front for [010] and [001]. The discrepancy between ψ and θ is larger in [001] than [010].At the weld center, the dendrite growth velocities of [010] and [001] are lower than those at the solid/liquid boundary. For case (A), there are obvious transition positions among the solidification interface with differences in the average dendrite velocity for the [001] orientation. The average dendrite growth velocity of the [010] and [001] orientations of weld2 are lower than the other cases near the solidification interface. For case (B), the solidification time is much less at high welding speeds, and dendritic arrays do not have sufficient time to establish steady state spacing. The average dendrite tip velocity in the [010] and [001] orientations are irregularly volatile along the solidification front at the highest welding speed. It is also observed that the welding speed affects the magnitude of the dendrite growth velocity for the [001] orientation near the solidification interface. For case(C), the average dendrite tip velocity for the [001] orientation monotonically increases with increase in laser power, and its magnitude is the largest near the fusion line with the highest laser power.

2.1.2.2. Role of welding parameters on stray grain formation

The area-weighted average values of stray grain formation tendency with different welding conditions is shown in Fig.6, and partial columnar growth with the value of $\overline{\overline{\Phi}}$ is below 0.5 and above 0.0066 with increase in arc current or welding speed. These welding parameters are beneficial for avoiding CET during the entire welding process. The effect of welding speed on $\overline{\overline{\Phi}}$ is more complex. The latter initially increases with increasing welding velocity before decreasing at higher speeds. This can be explained through the changes in temperature gradient transition with different welding speeds. As the welding speed is increased, the temperature gradient is generally affected by two opposing factors (Grong, 1997). Thus, the magnitude of $\overline{\overline{\Phi}}$ will subsequently decrease with a further increase in the welding speed. The results from Anderson et al. (2010) and Vitek (2005) are similar to those illustrated here, in which the fraction of stray grain formation is generally observed to reach the maximum at an intermediate speed, and then always decreases as the speed increases.

Hitherto, literature mainly focused on wide and shallow pool shapes and higher laser power conditions were omitted due to limitations in simulation and method (Anderson et al., 2010; Gäumann et al., 2001;Vitek,2005).From the investigations of this model, the effect of higher laser power is slightly negative on SG formation. Laser power is the primary factor in weld penetration and weld pool geometry which determines the shape of the liquid/solid interface and the slope of the weld pool edges. The local angle ϕ along the solidification interface in the nail-head shaped weld contributes more to stray grain formation. Hence, the typical keyhole geometry in a hybrid pool is more prone to create CET in the weld pool
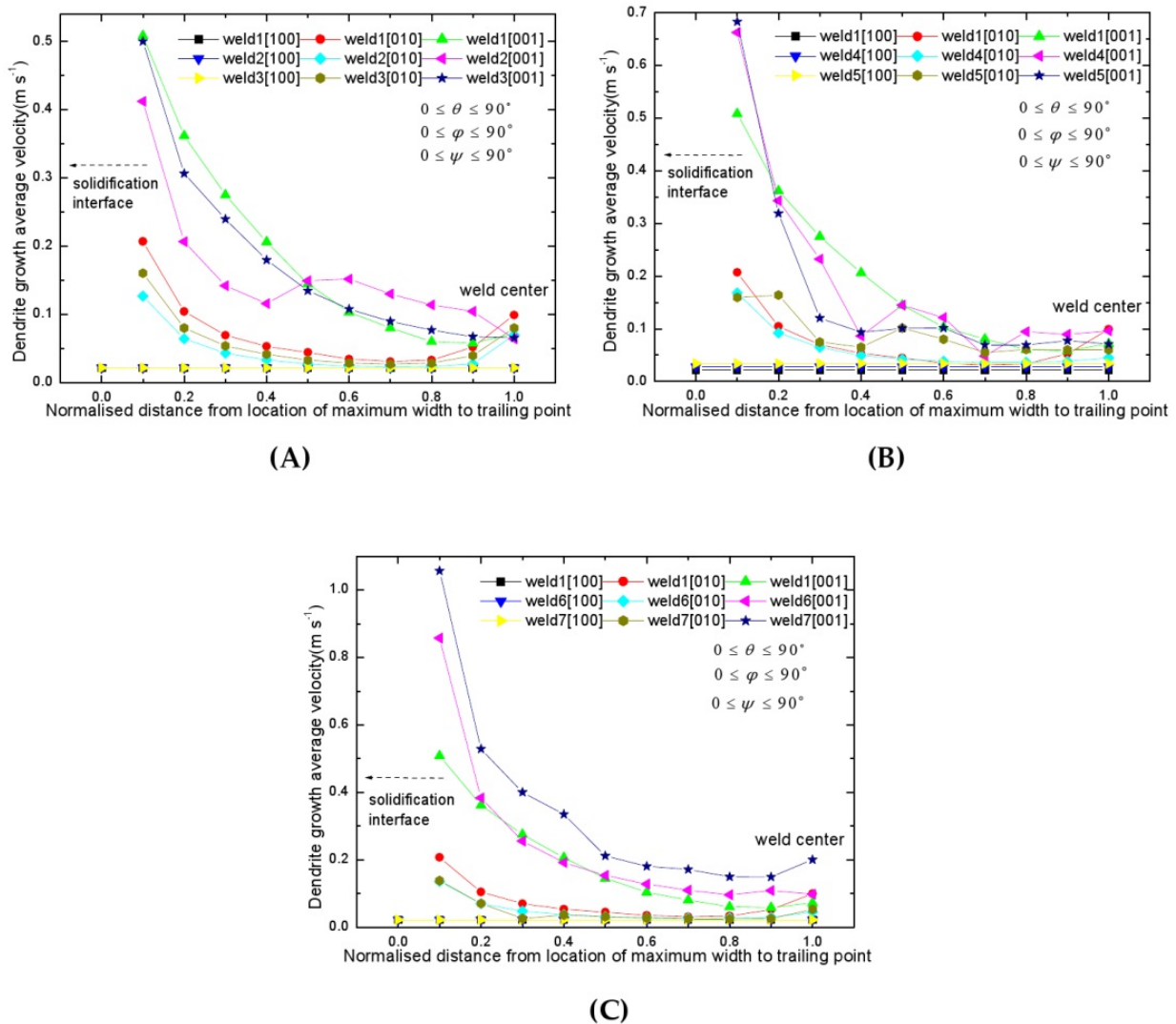

Figure 5. Dendrite tip velocity distribution around rear part of weld pool with different welding conditions, (A) variation of arc current, (B) variation of welding velocity, (C) variation of laser power (Gao&Ojo,2012a)
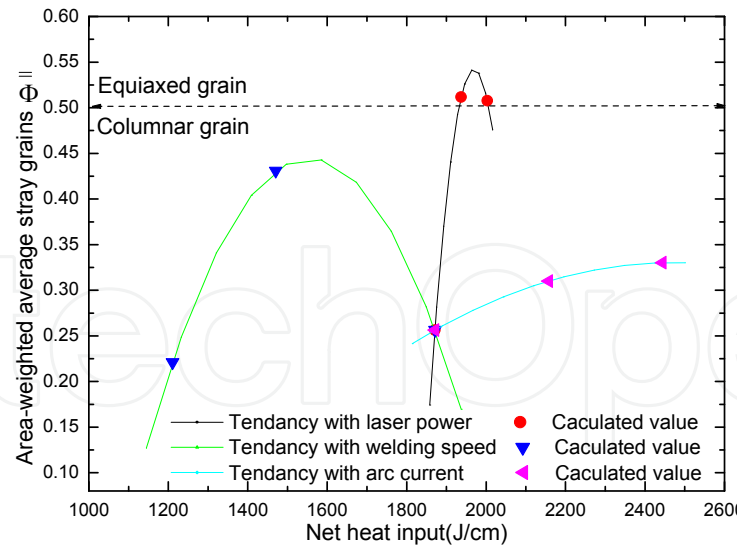
Figure 6. Area-weight average values of stray grain formation distribution as a function of heat input(Gao&Ojo,2012a)

when considering the distribution of Φ in the three directions from the above simulation, whereas the net effect of higher laser power on CET can be verified by the experimental work of Anderson et al. (2001), who used similar welding power intensity with an electron beam.

From the different tendencies of $\overline{\overline{\Phi}}$ summarized by the calculated value, higher welding speed and lower arc current or laser power ameliorate to minimize/avoid stray grain formation. In contrast, slower welding speed and higher arc current or laser power exacerbate stray grain formation, and abundant equiaxed dendrite will be yielded. Based on the above analysis, welding conditions should be optimized to minimize the overall likelihood of forming stray grains.

2.2. Liquation cracking modeling for polycrystalline superalloys welding

2.2.1. Mathematical model description

In consideration of tractable object symmetry, a 1/2 model including the weld metal, deposition filler material and base metal is adopted. A sequential thermal-mechanical finite element analysis is performed in present study based on ANSYS 13 code. Specifically, 2D thermal solid plane55 is used to simulate the temperature field and 2D structure element plane42 is then used to calculate the stress-strain field with the nodal temperature extracted from the thermal analysis as the load. All the material properties used in the model are displayed in Fig.7.

In this model, the laser-GMA hybrid process employs heating the base metal in a localized zone with sequent transient heat sources. The effect of the synergistic interaction between laser and GMA on the heat flux distribution is not considered in this simulation. The distribution of laser beam energy is assumed to be Rotary-Gauss body heat source, which is

suitable for nail-head shape with large depth to width ratio of molten pool along the workpiece thickness direction (Wu et al., 2004).The distribution of the GMA energy is assumed to be a Gaussian flux over the workpiece surface.
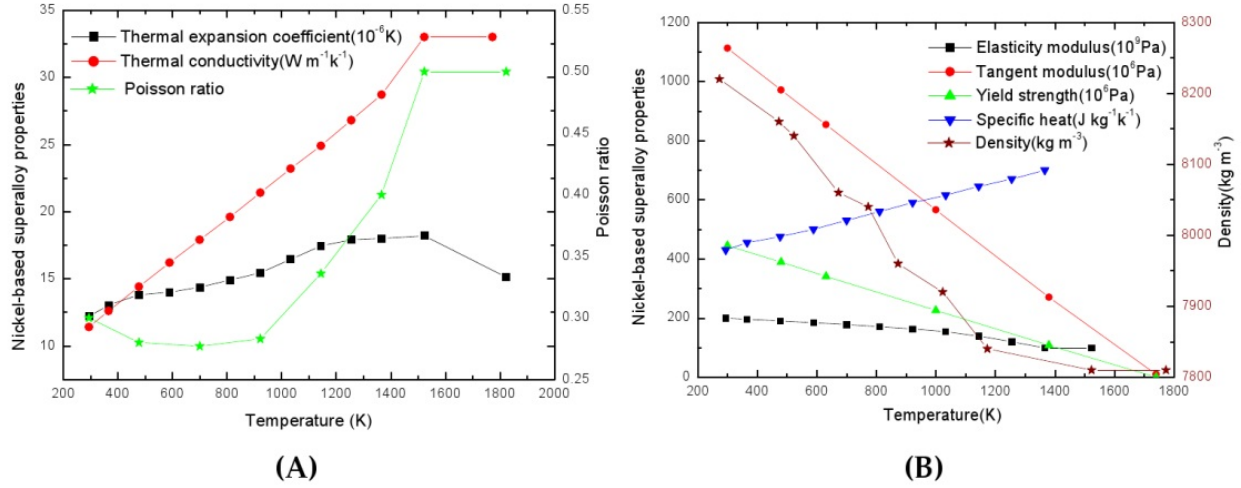

Figure 7. The physical and mechanical properties used for the simulation (Gao&Ojo, 2012b)

The crystallographic orientation of the dendrites is not taken into account and they are assumed to grow in a direction that is always perpendicular to the growth front. Local growth velocity of dendrite along the solidification front as a function of undercooling is represented by the following function (Hunziker et al., 2000):

$$v_{kin}\{\Delta T\} = a\Delta T^n \tag{18}$$

where n=3.05, a=1.2754×10^{-7}ms^{-1}K$^{-3.05}$ and the undercooled liquid is the region between the growth front and liquidus temperature. Using growth rate R and the temperature gradient G along the fusion boundary, the cooling rate (G×R) can be calculated.

For the case of nonlinear material, the definition of total strain is given:

$$\{\varepsilon\} = \{\varepsilon^{el}\} + \{\varepsilon^{th}\} + \{\varepsilon^{pl}\} \tag{19}$$

where ε^{el} is the elastic strain vector, ε^{th} is the thermal strain vector, ε^{pl} is the plastic strain vector but the creep strain vector and swelling strain vector are ignored.

As mentioned above, the thermal elasto-plastic material model, based on von Mises yield criterion, temperature dependent mechanical properties and linear kinematic hardening rule, is considered. The incremental forms of stress-strain relation are described as (Akbari & Sattari-Far, 2009; Chang & Lee, 2009; Kong & Kovacevic, 2010):

$$[d\delta] = [D^{ep}]\{d\varepsilon\} - [D^{th}]dT \tag{20}$$

$$[D^{ep}] = [D^e] + [D^p] \tag{21}$$

where dδ is the stress increment, dε is the strain increment, [D^e] is the elastic stiffness matrix, [D^p] is the plastic stiffness matrix, [Dth] is the thermal stiffness matrix and dT is the temperature increment. More information about this numerical model can be reviewed by referring to Gao (2012).

	Laser power (kW)	Arc power (kW)	Welding speed (m/min)	Time of laser heating (s)	Time of arc heating (s)	Time interval for hybrid (s)
Laser	2	-	3	0.012	-	-
Laser	4	-	3	0.012	-	-
Laser	6	-	3	0.012	-	-
Laser	4	-	2	0.018	-	-
Laser	4	-	4	0.009	-	-
Laser	4	-	6	0.006	-	-
Laser-GMA	2	4.75	3	0.012	0.05	0.02
Laser-GMA	4	4.75	3	0.012	0.05	0.02
Laser-GMA	6	4.75	3	0.012	0.05	0.02
Laser-GMA	4	4.75	2	0.018	0.075	0.03
Laser-GMA	4	4.75	4	0.009	0.0375	0.015
Laser-GMA	4	4.75	6	0.006	0.025	0.01

Table 3. Design laser and laser-GMA hybrid welding conditions (Gao&Ojo, 2012b)

Predictions for the cracking susceptibility have been estimated for a wide range of welding conditions. Two types of welding processing, three kinds of laser power and four kinds of welding speed have been investigated, which result in a total twelve laser fabrication conditions, as shown in Table 3.There is a time interval for laser-arc hybrid welding, which sequentially heats the base material due to the distance between laser beam and arc source.

2.2.2. Results and discussion

2.2.2.1. Weld pool solidification characteristics

The HAZ cracking in the waisted zone over the bead cross-section is attributed to the greater amount of grain boundary liquation during the cooling process. The solidification completion temperature of liquated grain boundary is around 1383K, which affects the Laves cluster dissolution and grain boundary liquid phase (Nishimoto et al., 2002). The shape of weld pool and cooling rate along localization fusion boundary derived from temperature isothermal are shown in Fig.8. The abscissa means the distance from the surface to the root of the weld bead along the fusion boundary. The left ordinate value indicates the weld geometry, which is the distance from the weld bead centerline and the right ordinate value is the cooling rate.
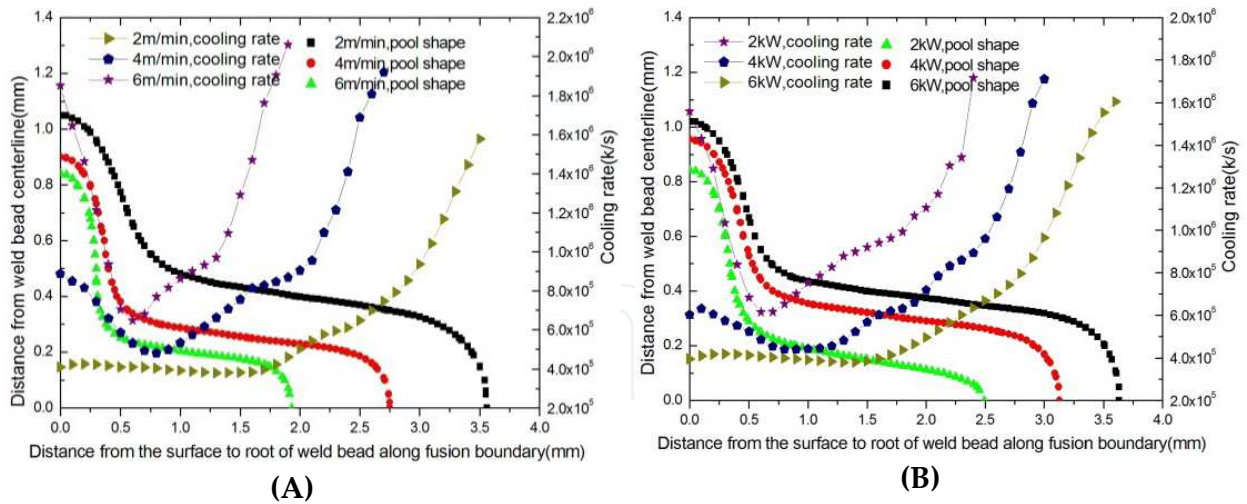
Figure 8. Correlation between the shape of weld pool and cooling rate with welding parameters for laser welding , (A) variation of welding speed, (B) variation of laser power

The results indicate that the cooling rate is a function of position along the fusion boundary among the weld fusion zone and varies simultaneously with the penetration shape. The shape decay of temperature in the surface region is attributed to the heat loss from the surface region due to heat transfer of conduction and convection in this region. Temperature decay in the initially high temperature region at the root of the keyhole during the laser beam moving away, which is due to the attainment of high temperature gradient in this region, results in faster solidification. The neck zone over the bead cross-section is more liable to heat stagnation than in other regions and undergoes lower cooling rates than other parts. That means that the maximum solidification time exists at the neck zone of the weld shape and the minimum solidification time occurs at the root of the keyhole. Thus, there is obvious solidification time transition region along the fusion boundary line. There is a steep cooling rate in the vicinity of the neck zone. With an increasing welding speed, the cooling rate in the neck zone gets steeper and weld pool geometry substantially decreases, respectively. Correspondingly, the shapes of weld pool synchronously enlarge with a laser power increase and the concomitant cooling rates considerably decrease.

Correlation between weld pool geometry and cooling rate of the hybrid pool characteristic are shown in Fig.9. The difference in these relationships between laser and hybrid laser arc welding are compared, and several conclusions can be drawn from the proposed study. First, with incorporating the effect of filler material on the weld bead cross-section, the weld pool geometry variation with welding speeds of laser hybrid welding are different from that of laser welding. Employing an additional heat and deposition metal lead to an extended region of weld width and increased neck zone radius of curvature. The volume of weld filler metal strongly depends on the welding speed and decreases with an increasing welding speed. Second, the rational link between cooling rate and weld pool geometry suggest that the neck zone over bead cross-section is more liable to heat stagnation and has larger solidification time, therefore, the minimized cooling rate occurs more readily at locations where it is underside of neck zone, which is especially observed in the neck-like waisted

zone of lower heat input of laser-GMA hybrid welding as well as laser welding. Third, laser-GMA hybrid welding alters the temperature distribution of the weld fusion zone and substantially enhances the cooling rate near the weld bead neck zone. The magnitude of cooling rate is lower than that of laser welding. Cooling rate attains low value in the region of neck zone due to higher solidification time, and obviously increases near the bottom of the keyhole. The relationship between the weld pool shape and the cooling rate elucidates clearly localized solidification behavior and enables the cause of liquation cracking to be explained.
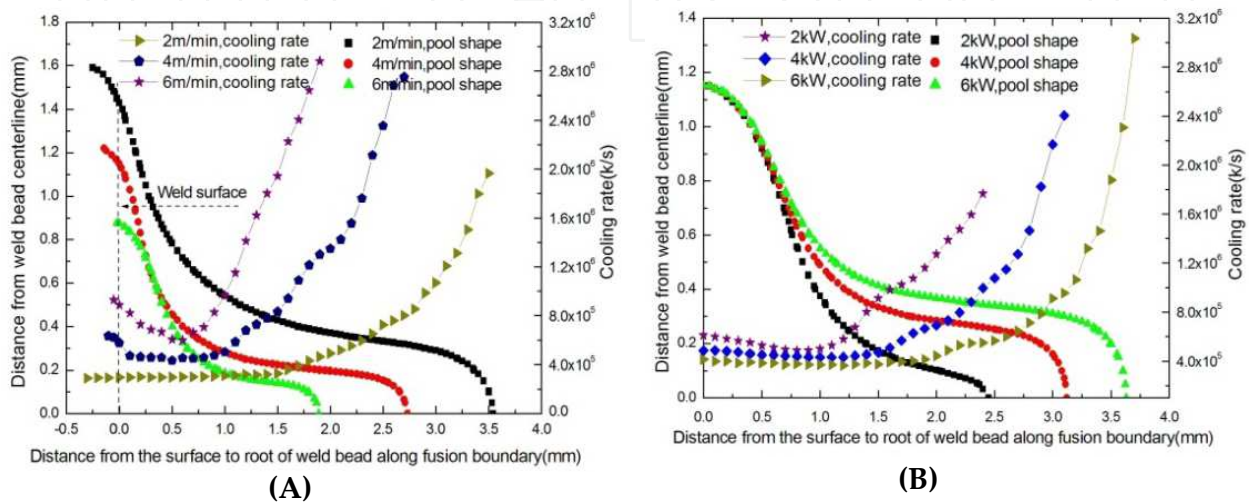

(A) **(B)**

Figure 9. Correlation between the shape of weld pool and cooling rate with various welding conditions for laser-arc hybrid welding, (A) variation of welding speed, (B) variation of laser power

2.2.2.2. HAZ cracking analysis

Constitutional liquation theory and grain boundary segregation mechanism are associated with weld HAZ liquation cracking. Nishimoto et al (2002) explained the liquation cracking mechanism in laser welds of Inconel 718. The molten liquid of the Laves phase eutectically is liquated at a temperature below the solidus temperature of the matrix and infiltrates along the grain boundaries. Tensile plastic strain/stress induced by thermal shrinkage is imposed on the liquid film during the subsequent cooling process and cracking will occur with an attendant buildup of higher strain/stress across the grain boundaries.

Despite the fact that the HAZ cracking metallurgical mechanism of nickel-base alloy is revealed, the limited information is available in the literature about the explanation of the relationship between welding conditions and cracking susceptibility during the laser and hybrid laser-GMA welding.

For the purpose of comparison of crack susceptibility with various welding conditions and different welding types, von Mises stress and 1st principal strain are not sensitive to reflect these discrepancies (Gao, 2012). Quantitative evaluation of solidification crack with behavior of ductility near the solidification boundary can be calculated by crack susceptibility strain rate, which is represented:

$$\dot{\varepsilon} = \frac{\varepsilon_1}{t_s} \tag{22}$$

where ε_1 denotes total 1st principal strain along the fusion boundary, t_s denotes the lapse time of solidification boundary from liquidus temperature to crack sensitive temperature, 1383K.
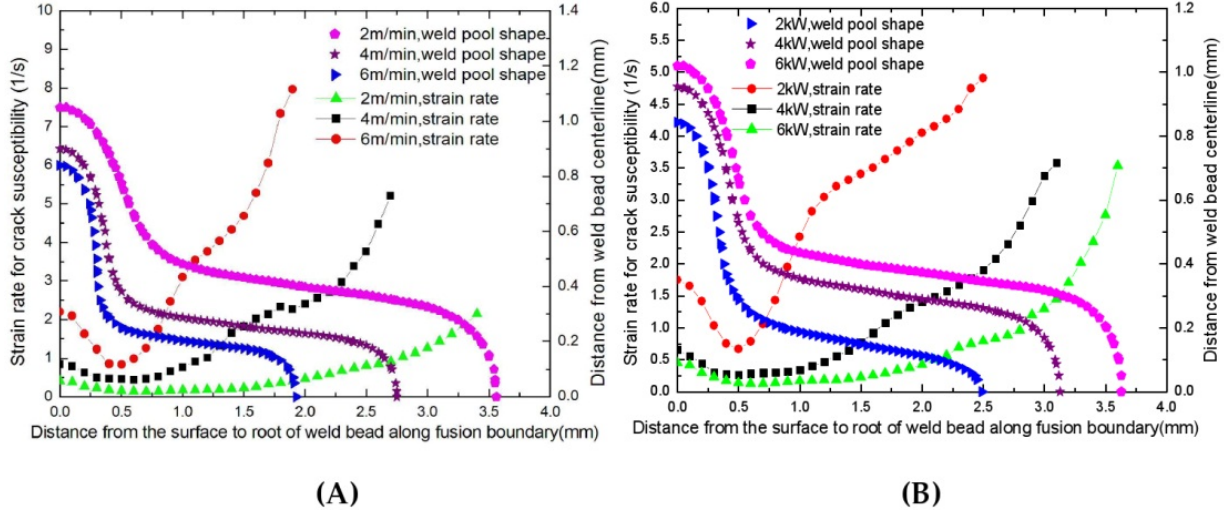

Figure 10. Correlation between the shape of weld pool and strain rate with various welding conditions for laser welding, (A) variation of welding speed, (B) variation of laser power(Gao&Ojo, 2012b)

Relations among crack susceptibility strain rate and pool shape of laser weld are shown in Fig.10. As a whole, it is worth noting that the value of the geometry of weld pool is nearly in the same order of the crack susceptibility strain rate, and the curve shapes of crack susceptibility strain rate conspicuously change with various welding conditions. It should be noticed that there is a concave shape, which suddenly decreases and then increases in the strain rate curve adjacent to the neck region of weld pool shape that means it is more susceptible to initiate crack in the stage of solidification. After the neck zone, strain rate increases until it is at the root of the keyhole and reaches a maximum value. The reason for this gradual increase in strain rate is thought to be due to the interaction between strain distribution and solidification characteristic within the weld pool. It can be estimated that greater welding speed and smaller laser power, namely less heat input results in the steeper curve of crack susceptibility strain rate, which is prone to engender and propagate cracks in the neck zone. Thus, the crack susceptibility strain rate itself is a major parameter determining the tendency of crack susceptibility.

As mentioned before, the effects of the welding conditions on the solidification crack susceptibility are interrelated. In contrast, laser–GMA hybrid welding can minimize the risk of variation of strain rate in the neck zone of the weld bead, and the value of these ductility curves are obviously smaller than that of laser welding, as shown in Fig.11. The strain rate becomes sharp near the neck region with an increasing welding speed or decreasing laser power.
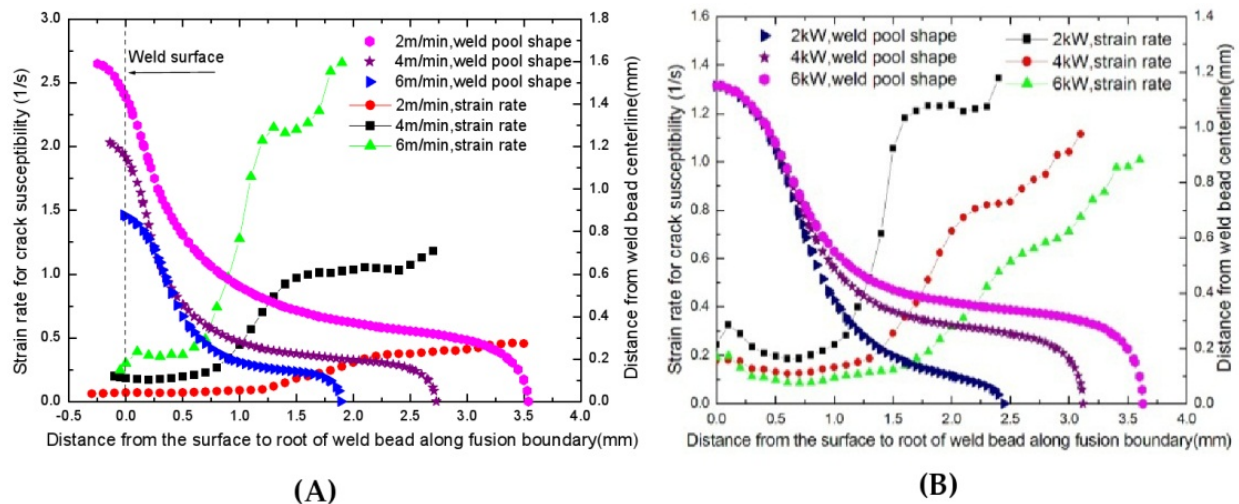
Figure 11. Correlation between the shape of weld pool and strain rate with various welding conditions for laser-arc hybrid welding, (A) variation of welding speed, (B) variation of laser power(Gao&Ojo, 2012b)
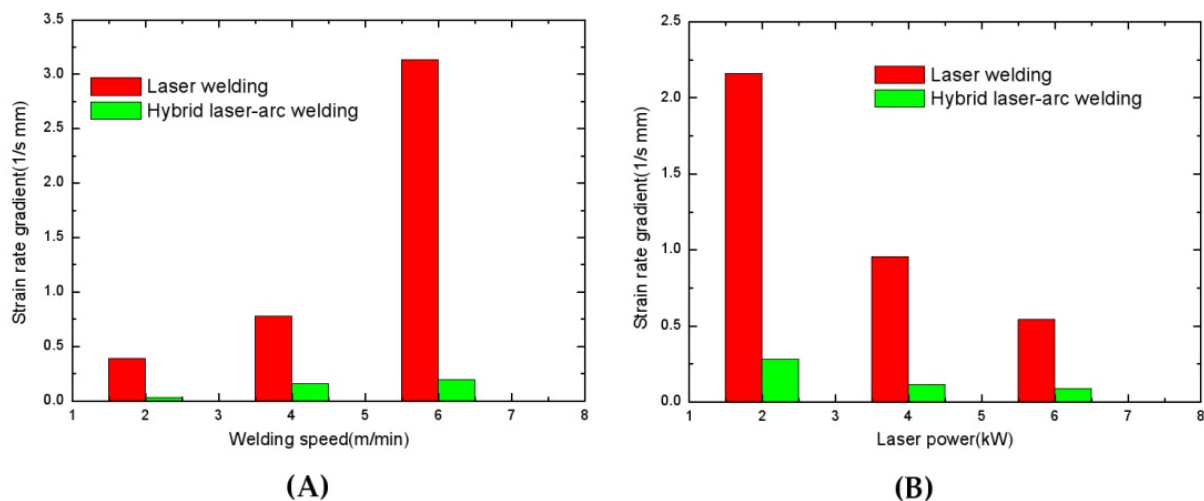

Figure 12. The strain rate gradient near the neck region with different welding conditions, (A) variation of welding speed, (B) variation of laser power

Comparison of strain rate gradient near the neck region under different welding conditions is illustrated in Fig.12. It is worth noting that the strain rate gradient decreases with heat input increase. The values of strain rate gradient of laser welding are on the whole higher than those of hybrid laser arc welding. It clearly reveals that laser welding is more susceptible to liquation cracking and the crack is located more in the neck region during low heat input. Therefore, the solidification cracking relating the liquid film stage in cracking sensitive temperature range can be explained from the view point of the contribution of strain rate gradient. From the above results, using strain rate gradient for evaluation of the susceptibility to HAZ liquation cracking provides theoretically understanding of how laser-arc hybrid welding produces less susceptibility to liquation cracking compared to laser welding as previous reported experiment results (Stelling et al., 2005).

3. Conclusions

These models provide valuable insight into the metallurgical and mechanical driving force for cracking. These results will be used to predict the effect of welding conditions on the potential for weld solidification cracking and HAZ liquation cracking and to interpret the experimental results during laser-GMA hybrid welding single-crystal and polycrystalline nickel-base superalloys. It should be noted that higher welding speed and lower laser power or arc current are beneficial for minimizing stray grain formation for laser-GMA welding single-crystal nickel-base superalloys , but generally lower heat input exacerbate HAZ liquation cracking for laser-GMA welding polycrystalline nickel-base superalloys. These promising results will also be used to identify preferred welding conditions that minimize stray grain formation, local stress-strain and associated cracking. For the future research, many efforts will focus on the different welding parameters on the cracking trend with optimized tactics and substantiate them by experiments.

For the solidification cracking modeling of welding of single-crystal nickel-base superalloys, there are some conclusions:

1. In almost all cases, the cooling rate is higher at the maximum width of the fusion boundary and at the bottom of the keyhole, while lower at the weld centerline and weld crown solid/liquid boundary. Meanwhile, it is shown that the finer arm spacing is always found near the solid/liquid boundary of the weld crown or the weld root, and the coarsest structure occurs in the center of the weld crown;

2. The average dendrite tip velocity of the [001] orientation is much greater than that of [010], and the latter is higher than that of [100] near the solidification interface for the (001) ∥ [100] orientations. At the weld center, the average dendrite growth velocity of [010] and [001] is lower than that at the solid/liquid boundary;

3. Higher welding speed and lower laser power or arc current are beneficial for minimizing stray grain formation, when taking into consideration, on average, the tendency for stray grain formation over the entire weld pool;

   For the HAZ liquation cracking modeling of welding of polycrystalline nickel-base superalloys, there are also some conclusions:

4. The neck zone radius of curvature in the laser hybrid pool is larger than that of the laser pool, which means the neck region is more liable to heat stagnation and has a smaller cooling rate. The minimized cooling rate occurs more readily at the underside of the neck zone, which is observed in the neck-like waisted zone of laser-GMA hybrid welding as well as laser welding;

5. Laser-GMA hybrid welding alters the temperature distribution of the weld fusion zone and substantially improves the cooling rate near the weld bead neck zone; the magnitude of cooling rate is lower than that of laser welding. The cooling rate attains low value in the region of neck zone due to higher solidification time and increases near the bottom of the keyhole;

6. The values of strain rate gradient near the neck region of laser welding are on the whole higher than those of hybrid laser-GMA welding. Laser welding is more susceptible to

liquation cracking and the crack is located more in the neck region during lower heat input compared to laser-GMA hybrid welding;

7.   The weld pool shape has a strong influence on the stress-strain pattern, and a neck weld pool shape can have a detrimental effect on the HAZ cracking behavior. Adding the arc heat source alters the strain distribution, and strain rate gradient provides theoretically understanding of how laser-GMA hybrid welding produces less susceptibility to liquation cracking compared to laser welding.

Author details

Zhiguo Gao
University of Manitoba, Canada

Acknowledgement

4. References

Akbari, D. & Sattari-Far, I. (2009). Effect of the welding heat input on residual stresses in butt-welds of dissimilar pipe joints. *International journal of pressure vessels and piping*, Vol.86, No.11, pp. 769-776

Anderson, T.; DuPont, J. & DebRoy, T. (2010). Origin of Stray Grain Formation in single-crystal superalloy weld pools from Heat Transfer and Fluid Flow Modeling. *Acta Materialia*, Vol. 58, No.4, pp.1441-1454

Banerjee, P. & Overfelt, R. (1999). Viscosity measurements of industrial alloys using the oscillating cup technique. *International Journal of Thermophysics*, Vol.20, No.6, pp.1791-1800

Bonifaz, E. & Richards, N. (2009). Modeling cast IN-738 superalloy gas tungsten arc welds. *Acta Materialia*, Vol.57, No.57, pp.1785-1794

Brooks, R.; Monaghan, B. & Barnicoat A. (1996). The Physical properties of alloys in the liquid and "Mushy" states, *International Journal of Thermophysics*, Vol.17, No.5, pp.1151-1161

Bussac, A. & Gandin, C. (1997).Prediction of a process window for the investment casting of dendritic single crystals. *Materials Science and Engineering: A*, Vol.237, No.1, pp. 35-42

Chang, K. & Lee, C. (2009). Finite element analysis of the residual stresses in T-joint fillet welds made of similar and dissimilar steels. *Int J Adv Manuf Technol*, Vol.41, No.3-4, pp.250-258

Claus,B.&Flemming,O.(2005). Review of laser hybrid welding. *Journal of Laser Applications*,Vol.17,No.1,pp.2-13

Dai, K. & Shaw, L. (2001). Thermal and stress modeling of multi-material laser processing. *Acta Materialia*, Vol.49, No.20, pp. 4171-4181

Dong, H.(2007). Analysis of Grain Selection during Directional Solidification of Gas Turbine Blades, *Proceedings of the Word Congress on Engineering 2007*, Vol.II WCE 2007, ISBN: 978-988-98671-2-6, London, U.K., July 2-4, 2007

Egbewande, A.; Buckson, R. & Ojo, O. (2010). Analysis of laser beam weldability of Inconel 738 superalloy, *Materials characterization*, Vol.61, No.5, pp.569-574

Farzadi, A.; Serajzadeh, S. & Kokabi, A. (2010) Investigation of weld pool in aluminum alloys: Geometry and solidification microstructure. *International journal of thermal sciences*, Vol. 49, No.5, pp.809-819

Gao, Z.; Wu, Y. & Huang, J. (2009). Analysis of weld pool dynamic during stationary laser-MIG hybrid welding. *Int J Adv Manuf Technol*, Vol.44, No.9-10, pp.870-879

Gao, Z. (2012).Numerical modeling to understand liquation cracking propensity during laser and laser hybrid welding (I).*Int J Adv Manuf Technol*, Doi:10.1007/s00170-012-3907-8,pp.1-13

Gao, Z. & Ojo, O.(2012a) Modeling analysis of hybrid laser-arc welding of single-crystal nickel-base superalloys, *Acta Materialia* ,Vol.60,No.6-7,pp.3153-3167

Gao, Z. & Ojo, O.(2012b) Numerical modeling of HAZ liquation cracking tendency during laser and hybrid laser-arc welding processes, *Journal of Materials Science Research* , Vol.1,No.2,pp.42-55

Gäumann, M.; Bezençon, C.; Canalis, P. & Kurz, W. (2001).Single-crystal laser deposition of superalloys: processing microstructure maps. *Acta Materialia*, Vol.49, No.6, pp.1051-1062

Grong, Ø. (1997). *Metallurgical Modeling of Welding*, The Institute of Materials, London, U.K.

He, X.; Elmer, J. & DebRoy, T. (2005). Heat transfer and fluid flow in laser microwelding. *J. Appl. Phys.*Vol. 97, No.8, pp.084909-084909-9

Hee, S.; Han, S.; You, C. & Sung, M. (2010). Analysis of residual stress on AH32 butt joint by hybrid CO_2 laser-GMA welding. *Computational materials science*, Vol. 49, No.2, pp.217-221

Hong, J.; Park, J.; Park, N.; Eom, I.; Kim, M. & Kang, C. (2008). Microstructures and mechanical properties of Inconel 718 welds by CO_2 laser welding. *Journal of materials processing technology*, Vol.201, No.1-3, pp.515-520

Hu, B. & Richardson, I. (2006). Mechanism and possible solution for transverse solidification cracking in laser welding of high strength aluminium alloys. *Materials science and engineering, A* ,Vol.429,No.1-2,pp.287-294

Hunt J. (1984). Steady state columnar and equiaxed growth of dendrites and eutectic. *Materials Science and Engineering*, Vol.65, No.1, pp.75-83

Hunziker, O.; Dye, D. & Reed, R. (2000). On the formation of a centerline grain boundary during fusion welding. *Acta Materialia*, Vol.48, No.17, pp. 4191-4201

Kong, F.& Kovacevic, R. (2010). 3D finite element modeling of the thermally induced residual stress in the hybrid laser/arc welding of lap joint. *Journal of Materials Processing Technology*, Vol.210, No.6-7, pp.941-950

Liu, W. & DuPont. J. (2004). Effects of melt-pool geometry on crystal growth and microstructure development in laser surface-melted superalloy single crystals.

Mathematical modeling of single-crystal growth in a melt pool (part I). *Acta Materialia*, Vol.52, No.16, pp.4833-4847

Liu, W. & DuPont. J. (2005). Effects of substrate crystallographic orientations on crystal growth and microstructure development in laser surface-melted superalloy single crystals. Mathematical modeling of single-crystal growth in a melt pool (Part II). *Acta Materialia*, Vol.53, No.5, pp.1545-1558

Liu, F.; Lin, X.; Yang, G.; Song, M.; Chen, J.& Huang, W.(2011). Microstructure and residual stress of laser rapid formed Inconel 718 nickel-base superalloy. *Optics & laser technology*, Vol.43, No.1, pp.208-213

Long, R.; Liu, W.; Xing, F. & Wang H. (2008). Numerical simulation of thermal behavior during laser metal deposition shaping. *Transactions of Nonferrous Metals Society of China*, Vo.18, No.3, pp.691-699

Luo, X.; Shinozaki, K. & Kuroki, H. (2002). Analysis of temperature and elevated temperature plastic strain distributions in laser welding HAZ study of laser weldability of Ni-base superalloys. Welding International, Vol.16, No.5, pp.385-392

Moore, P.; Howse, D. & Wallach, E. (2004). Microstructures and properties of laser/arc hybrid welds and autogenous laser welds in pipeline steels .*Sci Technol Weld Joining*, Vol. 9, No.4, pp.314-322

Nishimoto, K.; Woo, I. & Shirai, M. (2002). Analyses of temperature and strain distributions in laser welds study of the weldability of Inconel 718 cast alloy. *Welding International,* Vol.16, No.4, pp.284-292

Park, J.; Babu, S.; Vitek, J.; Kenik, E. & David, S. (2003). Stray grain formation in single crystal Ni-base superalloy welds. *Journal of Applied Physics*, Vol.94, No.6, pp.4203-4209

Pottlacher, G.; Hosaeus, H.; Kaschnitz, E. & Seifter, A.(2002) Thermophysical properties of solid and liquid inconel 718 alloy. *Scandinavian Journal of Metallurgy,* Vol.31, No.3, pp.161-168

Rai, R.; Roy, G& DebRoy, T. (2007). A Computationally Efficient Model of Convective Heat Transfer and Solidification Characteristics during Keyhole Mode Laser Welding. *J Appl Phys.*,Vol. 101,No. 05409,pp.1-11

Ral, R.; Palmer, T.; Elmer, J. & Debroy, T. (2009). Heat Transfer and Fluid Flow during Electron Beam Welding of 304L Stainless Steel Alloy. *Welding Journal*, Vol. 88, No.3, pp.54-61

Rappaz, M.; David, S.; Vitek, J. & Boatner, L. (1990). Analysis of solidification microstructures in Fe-Ni-Cr Single-Crystal welds. *Metallurgical Transaction A,* Vol.21A, No.6, pp.1767-1782

Ribic, B.; Palmer,T. & DebRoy,T. (2009). Problems and issues in laser-arc hybrid welding. *International Materials Reviews*, Vol.54, No.4, pp.223-244

Roy, G.; Elmer, J. & DebRoy, T. (2006). Mathematical modeling of heat transfer, fluid flow, and solidification during linear welding with a pulsed laser beam. *J. Appl. Phys.*Vol.100, No.3, pp.034903-034903-7

Stelling, K.; Boellinghaus,Th.; Lammers,M. & Schobbert, H. (2005). Laser plasma power hybrid welding in vertical-up and vertical-down positions, *Proceedings of the 7th*

international conference on trends in welding research, pp. 121-126,Callaway gardens resort, Pine mountains, Georgia, USA, May 16-20,2005

Vitek. J. (2005). The effect of welding conditions on stray grain formation in single crystal welds-theoretical analysis. *Acta Materialia*, Vol. 53, No.1, pp., 53- 67

Wang, N.; Mokadem, S.; Rappaz, M. & Kurz, W. (2004). Solidification cracking of superalloy single- and bi-crystals. Acta materialia, Vol.52, No.1, pp.3173-3182

Wu, S.; Zhao, H.; Wang, Y. & Zhang, X. (2004). A new heat source model in numerical simulation of high energy beam welding. *Transactions of the china welding institution*, Vol.25, No.1, pp.91-94

Yann, D.; Eric, L. & Corinne, A. (2010). Numerical modeling of Inconel 738LC deposition welding: prediction of residual stress induced cracking. *Journal of Materials Processing Technology*, Vol.210, No.14, pp.2053-2061

Yilbas, B.; Akhtar, S. & Karatas, C. (2010). Laser surface treatment of Inconel 718 alloy: Thermal stress analysis. *Optics and Lasers in Engineering*, Vol.48, No.7-8, pp.740-749

Zeng, D. (2006). Annular beam shaping and optical trepanning, In: *Doctor of Philosophy*, 22.02.2012, Available from
http://etd.fcla.edu/CF/CFE0001333/Zeng_Danyong_200612_PHD.pdf